Remote Sensing of Environment 251 (2020) 112111

Contents lists available at ScienceDirect

Remote Sensing of Environment

journal homepage: www.elsevier.com/locate/rse

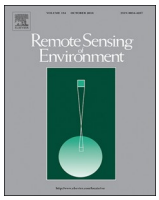

On the impact of C-band in place of L-band radar for SMAP downscaling

Elaheh Ghafari[a,b,*], Jeffrey P. Walker[a], Narendra N. Das[c], Kamran Davary[b], Alireza Faridhosseini[b,d], Xiaoling Wu[a], Liujun Zhu[a]

[a] Department of Civil Engineering, Monash University, Melbourne, Australia
[b] Department of Water Engineering, Ferdowsi University, Mashhad, Iran
[c] Jet Propulsion Laboratory, NASA, California Institute of Technology, Pasadena, CA 91109, USA
[d] Centre for Water Systems, College of Engineering, Mathematics and Physical Sciences, University of Exeter, Exeter, United Kingdom

ARTICLE INFO

Keywords:
Downscaling
Brightness temperature
Backscatter
L-band
C-band
SMAP
Sentinel-1A
SMAPEx

ABSTRACT

The National Aeronautics and Space Administration (NASA) Soil Moisture Active Passive (SMAP) mission was launched on 31st January 2015, with the aim of providing global soil moisture maps at 9 km spatial resolution by combining L-band radar and radiometer observations. However, after the SMAP radar became inoperable, NASA decided to utilize the Sentinel 1A/1B C-band SAR data in its place. The new version of baseline brightness temperature (*Tb*) downscaling algorithm for SMAP is tested using L-band airborne data to evaluate the capabilities of the C-band Sentinel-1A SAR relative to L-band radar data in downscaling the SMAP *Tb* for achieving high resolution brightness temperature. In this study, the downscaling algorithm used L-band airborne Synthetic Aperture Radar (SAR) backscatter (σ) collected from the fifth Soil Moisture Active Passive Experiment (SMAPEx-5) in south-eastern Australia to downscale 36 km L-band SMAP radiometer *Tb* pixels to 3 km and 9 km. The downscaling results were then compared with the published results using Sentinel-1A C-band backscatter, and evaluated against airborne 1 km resolution L-band passive microwave brightness temperature collected from SMAPEx-5. The results show that for vertical polarization the average Root Mean Square Error (*RMSE)* of downscaled *Tb* when compared with reference airborne *Tb* across 4 days at 9 km resolution were 4.9 K for L-band and 6.0 K for C-band, and increased to 9.3 K for L-band and 9.6 K for C-band at 3 km spatial resolution. Moreover, the correlation coefficient *(R)* of downscaled and reference *Tb* across the 4 days was 0.92 for L-band and 0.88 for C-band at 9 km, decreasing to 0.75 for L-band and 0.72 for C-band at 3 km spatial resolution. Accordingly, the *RMSE* increased and the correlation coefficient decreased when using C-band radar data in place of that at L-band. However, overall there is expected to be only a slight decrease in performance of the downscaling algorithm by using the Sentinel 1A data in place of the SMAP radar.

1. Introduction

Soil moisture is a fundamental parameter for monitoring the global water, energy and carbon cycles between the land surface and the atmosphere, especially in hydrology, meteorology and agriculture (Falloon et al., 2011; Seneviratne et al., 2010). Due to the necessity to access soil moisture observations globally, remote sensing technology has been adopted as an appropriate alternative to ground soil moisture measurement approaches (Entekhabi et al., 2010; Kerr et al., 2012).

The most widely accepted method to measure near surface soil moisture is passive microwave remote sensing at L-band, as it has the capability of observing data in all weather conditions, a direct relationship between soil moisture and brightness temperature, and minimal vegetation, surface roughness and atmospheric effects (Ulaby et al., 1981). While passive microwave remote sensors have the capability to estimate soil moisture accurately (Colliander et al., 2017), the spatial resolution is approximately 40 km, which is not adequate for hydrometeorology, hydrology or agricultural applications (Leese et al., 2001). The greatest advantage of active microwave remote sensing is its high spatial resolution (Torres et al., 2012). However, it is hard to interpret the radar data for soil moisture due to its strong dependence on vegetation and surface roughness (Jagdhuber et al., 2019a). Moreover, the revisit time of such high resolution satellites is not able to meet the requirements of global coverage with 2 to 3 day temporal repeat (Walker and Houser, 2004). Accordingly, microwave radiometer downscaling algorithms have been developed to disaggregate the

* Corresponding author at: Department of Water Engineering, Ferdowsi University, Mashhad, Iran.
E-mail addresses: ghafarielaheh84@gmail.com (E. Ghafari), Jeff.Walker@monash.edu (J.P. Walker), narendra.n.das@jpl.nasa.gov (N.N. Das), farid-h@um.ac.ir (A. Faridhosseini), Xiaoling.Wu@monash.edu (X. Wu), Liujun.Zhu@monash.edu (L. Zhu).

https://doi.org/10.1016/j.rse.2020.112111
Received 12 March 2020; Received in revised form 18 September 2020; Accepted 20 September 2020

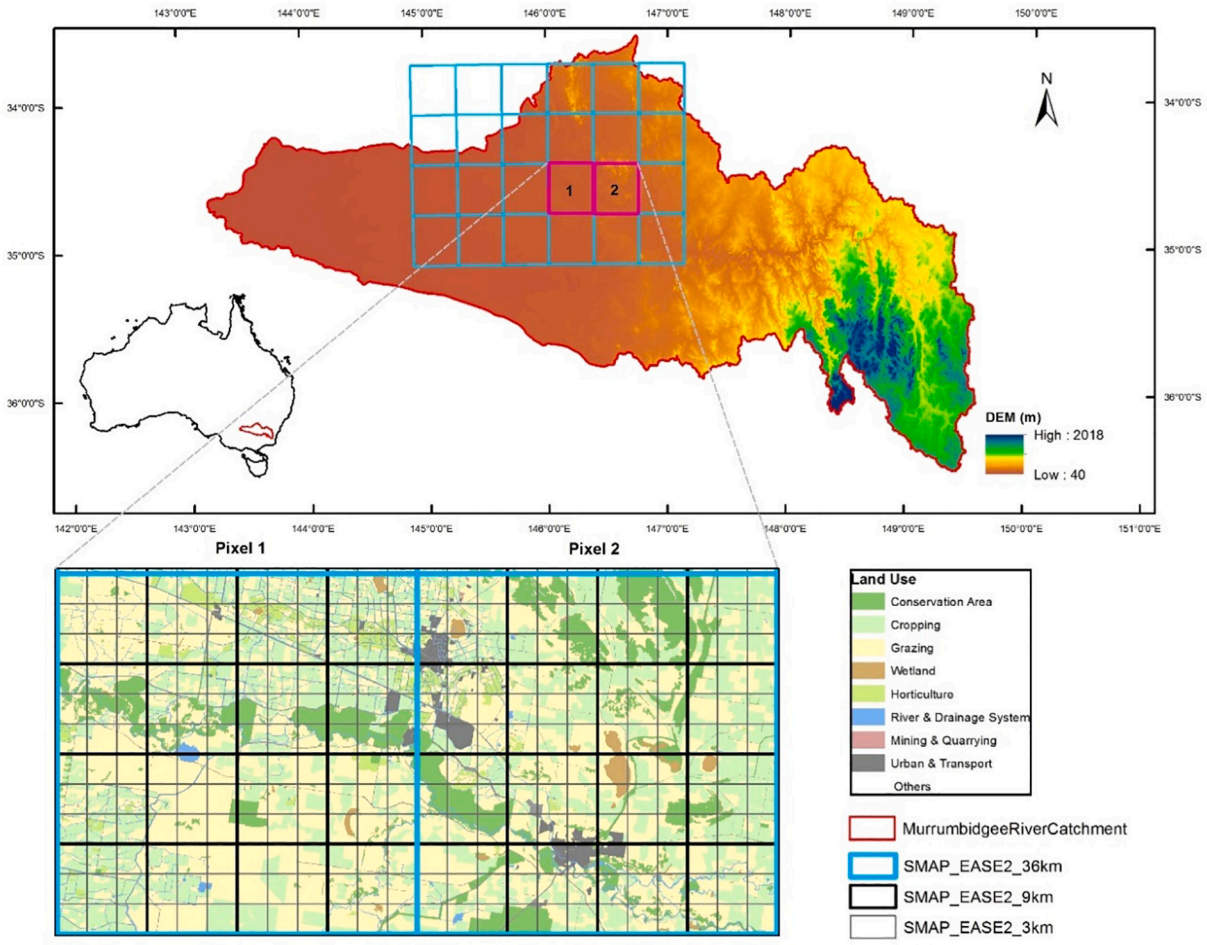

Fig. 1. Overview of the SMAPEx-5 study area in the Murrumbidgee catchment overlain with the Digital Elevation Model (DEM) and the SMAP EASE-2 36-km grid (top panel); Location and blow up of the selected SMAP EASE-2 36-km pixels (1 & 2), including the 9 km and 3 km scales overlain with the land use map (bottom panel).

coarse resolution observations using medium resolution ancillary, optical, radiometer or radar data (Jian et al., 2017; Sabaghy et al., 2018). However, there are some variations between these downscaling methods, with each having its own advantages and disadvantages. Generally, the oversampling-based downscaling techniques are more accurate in terms of *RMSE* than either the radiometer, radar or optical based techniques, due to their spatially detailed input requirements on soil surface attributes (Sabaghy et al., 2020; Sabaghy et al., 2018).

NASA's Soil Moisture Active Passive (SMAP) mission was launched on the 31st January 2015, with the explicit purpose of using L-band radar backscatter observations at 3 km resolution to downscale the ~40 km radiometer data (Entekhabi et al., 2010). Several active passive downscaling approaches have been proposed, such as the "old" (Das et al., 2014) and "new" (Das et al., 2019) versions of the SMAP baseline downscaling algorithm, SMAP "optional" downscaling algorithm (Das et al., 2011), "change detection" methods (Narayan et al., 2006; Piles et al., 2009), and "Bayesian merging" method (Xiwu et al., 2006). Unfortunately, on the 7th July 2015, the SMAP radar encountered a failure and became unworkable. Hence, the SMAP project has explored a number of alternative approaches to recover the ability of SMAP to provide high resolution soil moisture estimates, including the use of active microwave observations from other satellites such as the Copernicus Project Sentinel-1A/1B C-band (5.405 GHz) synthetic aperture radar (SAR) (Yueh et al., 2016). Sentinel-1 has a similar orbit configuration to SMAP, overlapping its swath with an acceptable time difference and providing both the co-polarization and cross-polarization measurements needed for the SMAP active passive algorithm (Das et al., 2018). Despite some limited evaluation of the SMAP/Sentinel-1 products, the effect of replacing the designed L-band radar data with C-band data has not been made clear. Notably, the wavelengths at L-band and C-band are different, strongly affecting the backscatter response and penetration depth of the radar signal. L-band, having a longer wavelength than C-band, penetrates more easily through the vegetation canopy and interacts with a deeper layer of soil. Thus, the use of C-band in place of L-band may cause several limitations and decrease the accuracy, especially over vegetated areas. Accordingly, this study tested the assumption that the L-band backscatter data required by the baseline brightness temperature downscaling algorithm of the SMAP mission (Das et al., 2018) can be replaced by the C-band backscatter data provided by Sentinal-1A. Importantly, it makes an assessment of the accuracy impact on the downscaling algorithm by contrasting the C-band results with those from coincident L-band observations collected over the semi-arid region of the Soil Moisture Active Passive Experiments (SMAPEx-5) airborne field campaign (Ye et al., 2020). The brightness temperature of SMAP, downscaled from 36 km to 3 km and 9 km, were subsequently evaluated against airborne brightness temperature observations collected at 1 km resolution from SMAPEx-5.

2. Study area and data set

2.1. Study area

The Soil Moisture Active Passive Experiments (SMAPEx) comprise a series of five airborne field campaigns over an approximately six year

time frame (2010 to 2015) ((Panciera et al., 2014; Ye et al., 2020). These campaigns were designed to develop the algorithms to interpret the NASA SMAP mission soil moisture observations before launch and validate the SMAP soil moisture products after launch. To achieve these objectives, SMAPEx collected airborne data similar to SMAP observations together with in situ soil moisture and ancillary information. The fifth campaign (SMAPEx-5), which was used in this study for evaluating the use of C-band radar in place of L-band radar for SMAP downscaling, was undertaken in the Austral spring from 6th to 28th September 2015. During this campaign, airborne active and passive microwave data and field measurements coincident with the overflight of the SMAP and Sentinel-1 satellites were acquired. Detailed information on the experimental data set is available in (Ye et al., 2020), so only a summary of the pertinent information is provided here.

The selected study area in this paper includes two 36 km EASE-2 Grid SMAP pixels (36 km × 36 km nominal resolution), located in the Yanco area of the Murrumbidgee River catchment (34.67°S, 35.01°S, 145.97°E, 146.36°E) in south-eastern Australia (Fig. 1). The selected site (pixel 1 and 2) was chosen to evaluate the SMAP baseline downscaling algorithm by reason of its flat topography, variability in vegetation and soil, and availability of required satellite and airborne data (Ye et al., 2020). This site is located in a semi-arid region having minimal changes in elevation, with predominantly irrigated and dry cropping and grazing land use. As can be seen in Fig. 1, the middle and western parts of the selected area are dominated by grazing and irrigated croplands, and the eastern part are covered mostly by dryland cropping, including a large wetland in the center of pixel 2 and a water body in pixel 1. Some woodlands and conservation areas exist along the Murrumbidgee River. There are also some forest areas in the north east of pixel 2, and some urban area mostly in pixel 2. Accordingly, the pixels contain typical heterogeneous land cover conditions. During the SMAPEx-5 campaign, the soil moisture varied from saturated to dry, providing data for an ideal dry-down period. In addition, the cropping and grazing areas were covered mainly by wheat and dense grasses, respectively. The SMAPEx-5 campaign was conducted in the Austral spring season, having high growth rates of vegetation with vegetation water content up to ~2 kg/m^2 (Ye et al., 2019).

2.2. Campaign data set

The SMAPEx airborne instruments for L-band passive and active microwave remote sensing measurement included the Polarimetric L-Band Multibeam Radiometer (PLMR) and the Polarimetric L-band Imaging Synthetic Aperture Radar (PLIS), at 1.41 GHz and 1.26 GHz, respectively. The airborne data was scheduled to be collected three times per week over the three weeks long SMAPEx-5 experiment period, including eight flights in total. These flights were coincident with SMAP and several Sentinel overpasses, providing airborne radar and radiometer data over several of the SMAP radiometer 3 dB footprints. The passive radiometer brightness temperature observations collected using PLMR measured both *v* and *h* (vertically and horizontally) polarized emissions at nominal incidence angles of 7°, 21.5° and 38.5° on each side of the flight track at 1 km spatial resolution. Flights were undertaken between the local time of 3 AM and 9 AM, coincident with the nominal 6 AM descending SMAP morning overpass time. The calibration of PLMR was confirmed before and after each flight. The calibration accuracy for both horizontal and vertical polarization was less than 1.4 K, calculated by considering the sky and microwave absorber as cold and warm targets, respectively.

Incidence angle normalization was undertaken for the PLMR observations to the outer beam angle (38.5°), being close to the SMAP 40° incidence angle by the approach of Ye et al. (2015). The approach uses a 2-D Cumulative Distribution Function (CDF) matching technique to normalize the microwave observations (brightness temperature or backscatter) from the original incidence angles to a reference angle. The same cumulative distribution of observations at the original and reference incidence angles are considered to force the CDF of the normalized observations of the original observations to that of the reference observations under the assumption of equivalent land surface heterogeneity. Based on the investigation by Wu et al. (2015), the accuracy of incidence angle normalization through this CDF approach was 2.4 K for PLMR brightness temperature at 1 km resolution. Moreover, a polynomial regression method, which uses the ratio between the soil temperature of the actual time and the nominal 6 AM time, was applied to thermally correct the PLMR observations to the exact descending SMAP overpass time. The accuracy of the PLMR brightness temperature thermal correction is around ± 1.5 K (Ye et al., 2020).

The active radar surface backscatter observations were collected using PLIS at *hh*, *hv*, *vh* and *vv* polarizations. PLIS is Australia's only L-band Polarimetric airborne interferometric SAR system with the ability of measuring data at high temporal and spatial resolution (Zhu et al., 2018). The PLIS antennas were mounted at an angle of 30° from the horizontal to either side of the aircraft to obtain push broom imagery over a cross track swath of ± 45°, providing high resolution imagery across an ~2 km swath on either side of the flight track. Due to the SAR technology, no high resolution data is available for the approximately 2 km swath immediately under the flight track. During the SMAPEx-5 airborne measurements, parallel flight lines were used for SMAP footprint coverage flights over the target area, with the distances between flight lines designed to support the full coverage of PLMR. Accordingly, there are PLIS coverage gaps in the middle of the swath which needed to be overcome. Therefore, the impact of these gaps on the aggregated PLIS data was investigated. For this purpose, *vv*-polarization PLIS backscatter measured during the SMAPEx-3, where there was full radar coverage over a similar part of the study area, was analysed to understand the impact of the gaps.

In order to prepare the PLIS observations for evaluation of the downscaling methods, data collected during the SMAPEx-5 campaign were processed in terms of calibration, georegistration and angle normalization. The processing steps are described as follows. For calibration, two type of targets were used: i) a large forest area for polarimetric calibration once a day and ii) artificial reflectors including trihedral passive radar calibrators (PRCs) and polarimetric active radar calibrators (PARCs). The accuracy of calibration was obtained as 0.58 dB. The calibration process and algorithms have been completely described in Zhu et al. (2018). Georegistration of the PLIS images was performed using the Landsat-8 operational land imager (OLI) image acquired on the 30th September 2015 as reference. In addition, the normalization of PLIS incidence angle to the SMAP 40° was performed using the same approach as for the PLMR data (Ye et al., 2015). The accuracy of angle normalization for PLIS observations was found as ~0.8 dB at 1 km resolution (Wu et al., 2015). Prior to aggregation of PLIS backscatter observations from high resolution (10 m) to the required spatial resolutions (1, 3 and 9 km), hybrid spatial filtering (including a median filter and a filter based on standard deviation thresholds developed at NASA JPL) was applied to eliminate the effects of urban areas, constructions, and water bodies from the PLIS measurements (replicating the processing applied to the Sentinel-1 data).

Briefly, the hybrid spatial filtering was applied considering four steps: a) for each 1 km^2 grid cell within a given SMAP pixel the mean (m_i) and the standard deviation (s_i) of the PLIS backscatter was calculated, $i = 1 \ldots N_C$, where N_C is the number of 1 km^2 grid cells within the SMAP pixel. b) The mean standard deviation (*SM*) over all the s_i with $i = 1 \ldots N_C$ was computed. c) For all 1 km^2 grid cells with $s_i > SM$, a moving window median filter with sample window size of 9 × 9 was considered. d) For all 1 km^2 cells with $s_i \leq SM$, all PLIS values out of range $[m_i - SM: m_i + SM]$ were eliminated. A more detailed description of the filtering process can be found in Das et al. (2019).

The original SMAPEx-5 spatial resolutions of the PLMR brightness temperature and PLIS backscatter observations were 1 km and 10 m, respectively. However, for use in this study the PLIS data have been aggregated to 36 km, 9 km, 3 km and 1 km by linear averaging of pixels

within the specific grid. In addition, the PLMR data were upscaled to 3 km and 9 km by the same method to evaluate the SMAP brightness temperature downscaling algorithm at the desired spatial resolutions. As the PLIS observations have been averaged from 10 m to 1 km, and then up to 3 km and 9 km for both PLIS and PLMR observations, the expectation is that the errors described earlier from normalization would be further reduced, and so those would be conservative worst case estimates.

2.3. Satellite data set

Sentinel-1 was the first of the Copernicus Project satellite constellation commissioned by the European Space Agency, composed of two separate satellites (A and B), launched on 3rd April 2014 and 25th April 2016, respectively. Note that only Sentinel-1A data correspond to the study period used in this paper. The operational band of the Sentinel SAR sensors is C-band (5.405 GHz) with the interferometric wide swath (IW) acquisition mode being the type of data used for providing the backscatter observations to the active passive downscaling algorithm. NASA has utilized this sentinel data to produce a new product, SMAP L2_SM_SP (Level 2 SMAP/Sentinel Active Passive Soil Moisture). The SMAP L2_SM_SP product is derived using the Sentinel-1 radar backscatter from L2_S0_S1 (aggregated at 1 km resolution on the EASE-2 grid) and the 9 km gridding of the enhanced radiometer brightness temperature available in the SMAP L2_SM_P_E products. A complete description can be found in Das and Dunbar (2017), with the products being available at https://earthdata.nasa.gov. In this paper, the downscaled brightness temperature of the SMAP L2_SM_SP product was compared with the downscaled brightness temperature achieved from the "new" baseline downscaling algorithm of Das et al. (2019) at 3 km and 9 km resolution using L-band radar data from PLIS. Finally, the brightness temperature ($Tb_v(c)$) values of SMAP L2_SM_P, which are the average of fore- and aft-looking brightness temperature on the 36 km EASE-2 grid cell, were used as the original base data in the downscaling algorithm.

2.4. Experiment data set

Table 1 shows details on characteristics of the different sensors used in this study. Based on the availability of the Sentinel-1A data 4 days of the SMAPEx-5 campaign were selected, being September 9 (D1), 14 (D3), 22 (D6), 27 (D8), 2015, ("D" represents flight "Day"). The simulated SMAP data stream used in this study is shown in Fig. 2. According to previous research, σ_{vv} has shown the best correlation with T_{bv} (Wu et al., 2014). Moreover, Chan et al. (2016) found that T_{bv} showed the best soil moisture retrieval performance and so was used as the post-launch baseline retrieval algorithm. Therefore, the vertical polarization has been utilized for this research.

The SMAPEx-5 airborne flight schedule had been arranged to align with the overpasses of SMAP on multiple days as seen in Table 1. To minimize the effect of soil temperature variations from that of the SMAP overpass, each flight started at local time of approximately 2:20 AM and finished at approximately 9:40 AM, aligning the centre flight time with the SMAP overpass time of 6:00 AM (Ye et al., 2020). While SMAP and Sentinel-1 were not designed to have synchronized overpasses, SMAP and Sentinel-1 had the same overpasses on days D6 and D8. Moreover, there was a Sentinel-1 overpass within +24 h of SMAP observations on D1 and D3, allowing them to also be used.

2.5. Impact of coverage gaps

As mentioned earlier, the PLIS coverage includes gaps over the SMAPEx-5 flight area, located in the middle of the PLMR swaths. A sample of PLIS coverage gaps can be seen in Fig. 3. In order to investigate the impact of gaps on the aggregated SMAPEx-5 PLIS data, the PLIS backscatter measured during the SMAPEx-3 were analysed, having full radar coverage over a part of the study area with similar conditions. A total of three of the 9 flights from SMAPEx-3 were used for this purpose, including one at the start, middle and end of the campaign (September 4 (D1), 15 (D5) and 23 (D9), 2011). This data was used to represent a comparison of the backscatter for the case of full coverage without gaps and the coverage with the SMAPEx-5 gaps imposed. As shown in Fig. 3, the original 10 m resolution PLIS data from SMAPEx-3 had the SMAPEx-5 gaps applied and then aggregated to 3 km resolution. It can be seen from the difference plot that the values of backscatter data at full coverage and the coverage with gaps at 3 km resolution had approximately zero bias and an *RMSE* of 0.2 dB, which was less than the calibration uncertainty of PLIS. The results for the other two dates is included in Fig. 4, with a correlation between the original and gap-imposed data being 0.98. These results demonstrate that the gaps should not adversely impact the accuracy of using PLIS backscatter data for downscaling at 3 km and 9 km resolutions, and the impact of this can therefore be ignored.

3. Methodology

The original SMAP active passive baseline downscaling algorithm (Das et al., 2018; Das et al., 2014; Entekhabi et al., 2014) assumes a near-linear relationship between coarse resolution brightness temperature (*Tb*, in kelvin) and fine resolution backscatter coefficient (σ, in decibel) at the same incidence angle and time. The SMAP brightness temperature is downscaled through this relationship, and then the retrieved soil moisture obtained using the downscaled brightness temperature. This algorithm utilizes two parameters, β [K/dB] and Γ [dB/

Table 1
Summary of the original data set characteristics.

Sensor	Band	Frequency	Polarization	Incidence angle	Spatial resolution of product	Revisit frequency	Overpass dates used	Accuracy
SMAP radiometer	L-band	1.4 GHz	*h* & *v*	40°	36 km	2–3 days	09/09/2015 14/09/2015 22/09/2015 27/09/2015	1.3 K
Sentinel-1A	C-band	5.405 GHz	*hh*, *vv*, *hh* + *hv* & *vv* + *vh*	20°–45°	5 × 20 m	1–2 weeks	10/09/2015 15/09/2015 22/09/2015 27/09/2015	1 dB
PLMR	L-band	1.4 GHz	*h* & *v*	17°, 21.5° & 38.5°	1 km	2–3 days	09/09/2015 14/09/2015 22/09/2015 27/09/2015	1.4 K
PLIS	L-band	1.26 GHz	*hh*, *vv*, *hv* & *vh*	15°–45°	10 m	2–3 days	09/09/2015 14/09/2015 22/09/2015 27/09/2015	0.58 dB

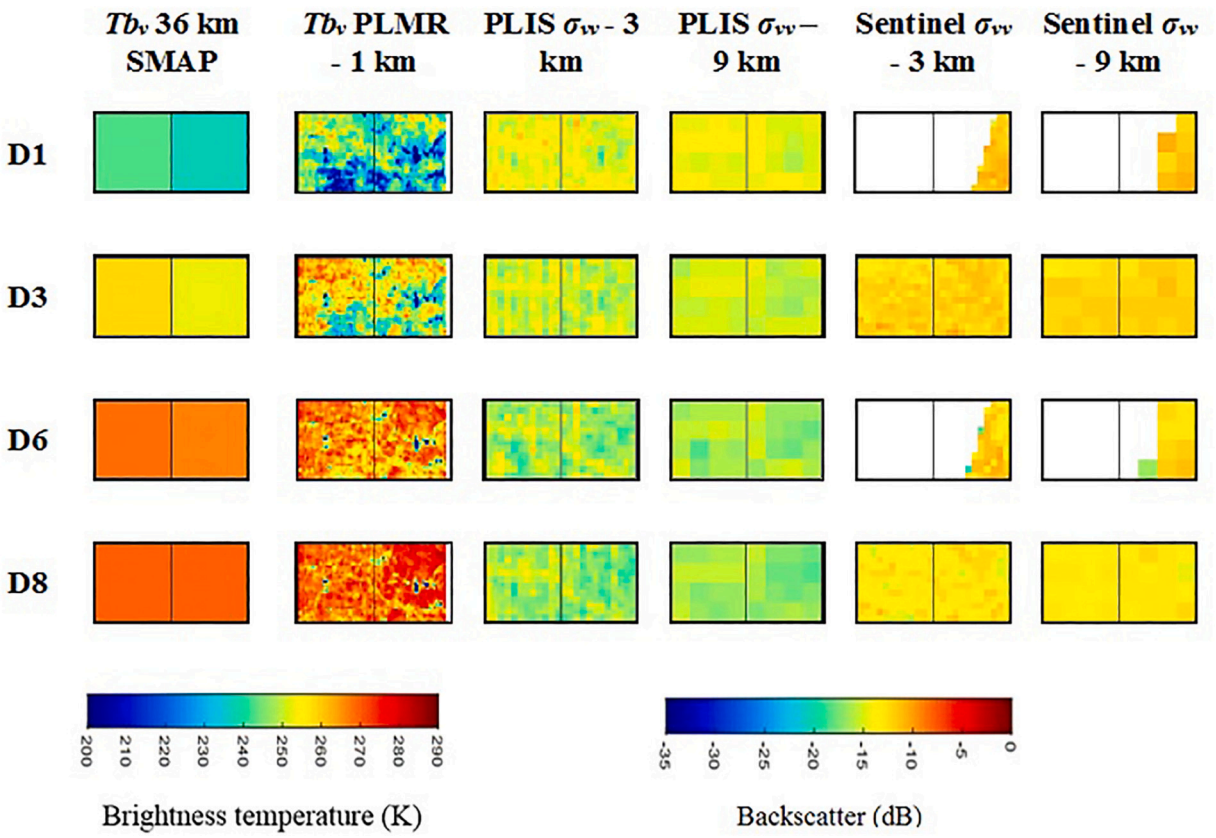

Fig. 2. Data sets used including SMAP L2_SM_P 36 km vertical brightness temperature (Tb_v), SMAPEx5 1 km PLMR vertical brightness temperature (*Tbv*), PLIS *vv* backscatter at 3 km and 9 km (σ_{vv}), and Sentinel-1A *vv* backscatter at 3 km and 9 km (σ_{vv}). Data are for pixel 1 & 2 across four days of the SMAPEx5 experiment (September 9 (D1), 14 (D3), 22 (D6) and 27 (D8), 2015).

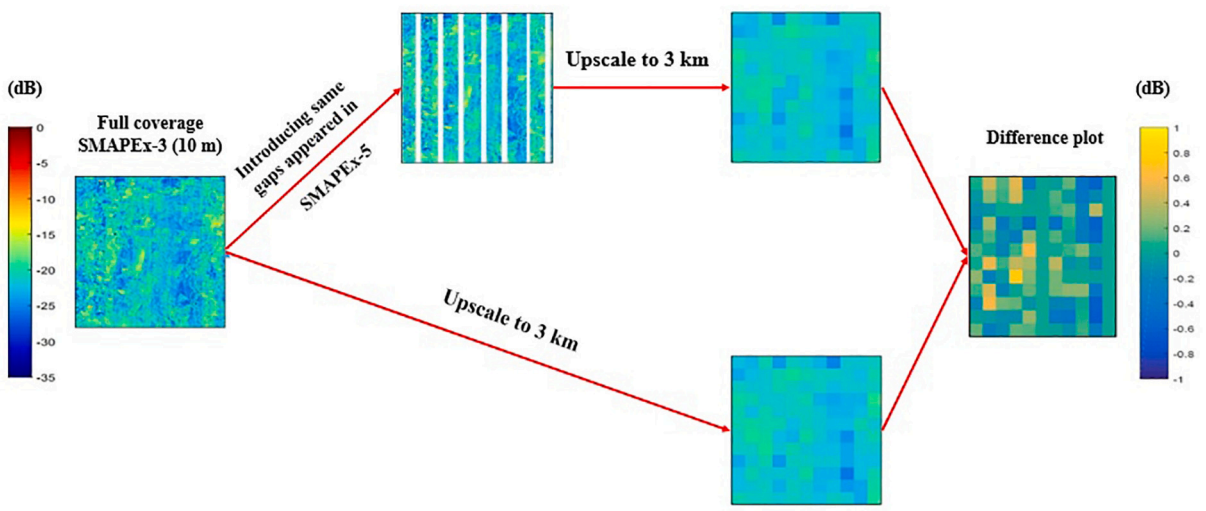

Fig. 3. The original SMAPEx-3 PLIS *vv*-polarization backscatter data at 10 m spatial resolution and with gaps imposed over D1 as an example. Data aggregated to 3 km with and without gaps, and the difference plot between backscatter data at full coverage and coverage with gaps at 3 km resolution is shown.

dB]. The parameter β of the original baseline downscaling algorithm depends on the vegetation cover conditions, vegetation type and surface roughness. This parameter is supposed to be constant during time and also homogenous over each 36 km grid cell. It is estimated by regressing the brightness temperature and backscatter observations at coarse resolution (C) from multiple overpasses. The parameter Γ indicates the vegetation and roughness heterogeneity of each radiometer pixel, and is determined using regression between aggregated co-polarized and cross-polarized radar backscatter for any particular overpass at the finest considered resolution (1 km in this research) (Das et al., 2018).

3.1. The SMAP active passive baseline downscaling algorithm

NASA recently introduced a “new” version of their downscaling algorithm with important changes in implementation (Das et al., 2019). In the new algorithm, an emissivity procedure was selected to replace the brightness temperature procedure, and the radar observations used

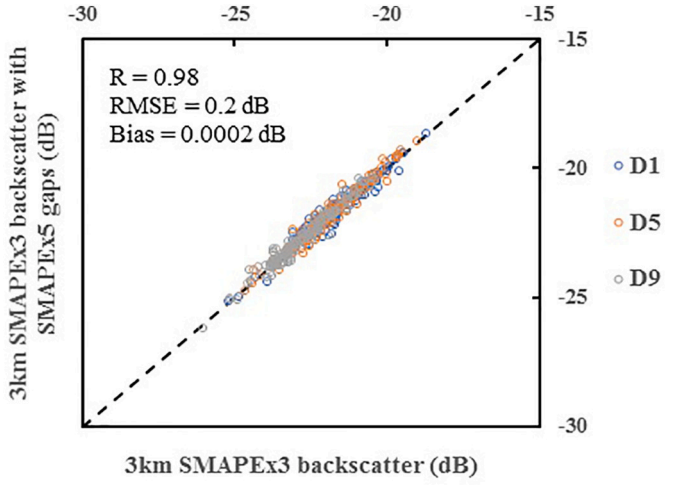

Fig. 4. Scatterplot of 3 km SMAPEx-3 backscatter vs 3 km SMAPEx-3 backscatter with the SMAPEx-5 gaps across the 3 dates of the three-week long SAMPEx-3 campaign, with the D1, D5 and D9 being September 4, 15 and 23, 2011 respectively.

in linear scale [−] rather than dB. The changes in implementation are intended to make this algorithm more suitable and efficient to Sentinel-1 than the "old" version because of differences in the overpass times of the radar and radiometer instruments. The reduced repeat interval of the Sentinel-1 also required other changes. Parameter estimation through time series was seen as inappropriate, as the brightness temperature and backscatter time series is too sparse, meaning there could be significant variations in vegetation cover and surface roughness conditions over the regression time period for β. In order to resolve the algorithm's reliance on sparse time series data, the snapshot retrieval approach of Jagdhuber et al. (2018) was adapted for estimating the covariation parameter between the SMAP brightness temperature and the radar backscatter observation. Accordingly, this new version of algorithm is used to provide the SMAP-Sentinel-1 products.

Since only four time instances are available in this study and to be consistent with the official SMAP-Sentinel product, the snapshot retrieval approach is also applied here to the L-band data from PLIS. This algorithm can be written as (Jagdhuber et al., 2018):

$$T_{b_p}(M_j) = \left[\frac{T_{b_p}(C)}{T_s} + \beta'(C).\{[\sigma_{pp}(M_j) - \sigma_{pp}(C)] + \Gamma.[\sigma_{pq}(C) - \sigma_{pq}(M_j)]\}\right] . T_s \quad (1)$$

where $T_{bp}(C)$ [K] is the coarse resolution brightness temperature (~36 km), and T_s [K] is the land surface soil temperature. The radar backscatter aggregated to coarse resolution is $\sigma_{pp}(C)$ [−] and $\sigma_{pq}(C)$ [−], being the co-polarized and cross-polarized backscatter in linear scale values, respectively. The radar backscatter $\sigma_{pp}(M_j)$ [−] and $\sigma_{pq}(M_j)$ [−] are at the desired medium resolution (3 km or 9 km, in this case). $T_{bp}(M_j)$ [K] is the disaggregated brightness temperature at medium resolution.

As shown in Eq. (1), the "new" SMAP baseline downscaling algorithm utilizes two parameters, $\beta'(C)$ and Γ, which completely control the brightness temperature disaggregation performance (Das et al., 2019). The parameter $\beta'(C)$ [−] is calculated based on the snapshot approach at each coarse (C) grid cell for each coincidence between the SMAP and SAR observation, and solely uses the remote sensing observations for retrieving the active passive microwave covariation. Moreover, it is dependent on land surface soil temperature and vegetation radiative transfer properties (Jagdhuber et al., 2018) and computed as (Jagdhuber et al., 2019a):

$$\beta'(C) = \frac{\frac{Tb_p(C)}{T_S} - (\gamma + (1-\omega)(1-\gamma))}{|S_{pp}(M_j)|^2 - \mu_{pp-pq}.|S_{pq}(M_j)|^2} \quad (2)$$

where ω [−] is the effective scattering albedo, $\gamma = e^{-\tau/\cos\theta}$ [−] is the vegetation loss term, including τ [−] as the vegetation opacity and θ [rad] as the incidence angle (in this study the SMAP angle of 40°) (Jagdhuber et al., 2018). The τ [−] parameter is an indicator of the vegetation cover characteristics, such as the vegetation water content (VWC). The numerator of Eq. (2) comprises passive microwave measurements and the physical land surface temperature, resulting in the measured surface emission minus the vegetation correction term. The second term of the numerator, known as the vegetation correction term, includes γ as the vegetation loss term plus $(1-\omega)(1-\gamma)$ as the vegetation emission term. The denominator, which is based on the active microwave observations, can be calculated through subtraction of the vegetation volume scattering from the co-polarized backscatter (Jagdhuber et al., 2019a). $|S_{pp}(M_j)|^2$ is the co-polarized backscatter such that $|S_{pp}(M_j)|^2 \equiv \sigma_{pp}(M_j)$, and $|S_{pq}(M_j)|^2$ is the cross-polarized backscatter such that $|S_{pq}(M_j)|^2 \equiv \sigma_{pq}(M_j)$. The vegetation volume scattering includes the cross-polarized backscatter and the projection of the cross-polarized backscatter onto the co-polarized backscatter. The projection, which is called the vegetation structure parameter, can be defined as $\mu_{pp-pq} = {\partial\,|S_{pp}(M_j)|^2}/{\partial\,|S_{pq}(M_j)|^2}$. It should be calculated the same as Γ of Eq. (1), through the linear regression between co-polarized and cross-polarized backscatter at fine scale (1 km in this research) within each radiometer resolution grid cell. Overall, the time series of $T_{bp}(C)$ and $\sigma_{pp}(C)$ are not required when the parameters $\beta'(C)$ and μ_{pp-pq} are estimated using this snapshot approach.

In order to calculate $\beta'(C)$ in this study, the snapshot approach based on Eq. (2) is used for every coincidence of SMAP and PLIS observations, with the estimation of β' being unique for any given day. In this study, $T_{bp}(C)$ of Eq. (2) is the average of the fore- and aft-looking SMAP vertical brightness temperature (L2_SM_P) at 36 km resolution. Estimation of β' is also dependent on T_s [K], ω [−], and $\gamma = e^{-\tau/\cos\theta}$ [−] of the 36 km grid cell. The parameter T_s [K], which is the land surface temperature based on GMAO GEOS-5 data, and the scattering albedo and vegetation loss parameters (ω [−], and τ [−]), have been extracted from the SMAP Level-2 product (L2_SM_P) at 36 km spatial resolution and 40° incidence angle (θ). For $|S_{pp}(M_j)|^2$ and $|S_{pq}(M_j)|^2$, the vv-polarized and vh-polarized radar backscatter observations from PLIS (σ_{vv} and σ_{vh}) at 10 m original resolution were spatially aggregated to the 36 km resolution SMAP EASE-2 grids. In addition, the slope of the linear regression between PLIS σ_{vv} and σ_{vh} at fine scale (1 km) was considered as μ_{pp-pq}. All PLIS backscatter observations were used as linear scale values. Finally, the parameter β' utilized in the downscaling process has been estimated using the above described observations through Eq. (2).

The parameter Γ [−] is estimated through the regression between the co-polarized and cross-polarized radar observations collected at fine spatial resolution within each radiometer grid cell. This parameter is calculated individually for each coarse grid cell and represents the spatial heterogeneity effects. It is estimated the same way in the new algorithm as in the old algorithm but in linear scale, such that $\Gamma \equiv \left[\frac{\partial\sigma_{pp}(M_j)}{\partial\sigma_{pq}(M_j)}\right]_C$. In this study, Γ was evaluated as the sensitivity of radar co-polarized to cross-polarized using PLIS σ_{vv} and σ_{vh} at fine scale (1 km) within each 36 km SMAP grid cell. The spatial deviation of cross-polarization backscatter (σ_{vh}) at C scale was used as the indicator of heterogeneity. Γ, which is unique for any particular overpass, projects the spatial deviation in σ_{vh} in the σ_{vv} space. This calculation can be additive or subtractive depending on the surface roughness and vegetation, with the magnitude of Γ being an indicator of the heterogeneity within the 36 km SMAP grid cell (Das et al., 2019). According to the baseline downscaling algorithm, the σ_{vh} variation can be converted to σ_{vv} variation by multiplying with the sensitivity Γ.

Overall, the magnitude of covariation β' decreases with increasing

soil roughness and vegetation water content due to the higher dynamic range of scattering compared to emission. This reduction is strongest for sparsely vegetated land or dry vegetation coverage conditions with VWC less than 1 kg/m^2. Soil roughness variations play the next most important role in covariation magnitude offsets, while the vegetation moisture variation does not change the covariation significantly (Jagdhuber et al., 2017). In addition, the covariation magnitude moves toward zero for VWC greater than 5 kg/m^2 (Jagdhuber et al., 2018). Since a dense or moist canopy leads to the attenuation of microwave signals of the soils, the covariation decreases with increased vegetation growth or wetness (Jagdhuber et al., 2019a; Jagdhuber et al., 2019b). With increased roughness and vegetation cover on the land surface, the parameter Γ increases, as the cross-polarized backscatter displays high sensitivity to vegetation and surface roughness (Das et al., 2011; Das et al., 2014).

3.2. Algorithm implementation

In this study, the term $[\sigma_{vv}(M_j) - \sigma_{vv}(C)]$ of Eq. (1) was calculated by considering the *vv*-polarization PLIS backscatter upscaled to medium resolution (3 km and 9 km) as $\sigma_{vv}(M_j)$ and the average of *vv*-polarization PLIS backscatter for the coarse resolution SMAP pixel as $\sigma_{vv}(C)$ for each selected SMAP 36 km pixel. The term $[\sigma_{vh}(C) - \sigma_{vh}(M_j)]$ was also calculated using the average of *vh*-polarization PLIS backscatter at coarse resolution SMAP pixel as $\sigma_{vh}(C)$ and the *vh*-polarization PLIS backscatter upscaled to medium resolution as $\sigma_{vh}(M_j)$ for each SMAP 36 km pixel. Then, the 36 km spatial resolution SMAP vertical brightness temperature ($T_{bv}(C)$) was downscaled to 3 km and 9 km ($T_{bV}(M_j)$) using backscatter (σ_{vv} and σ_{vh}) provided by the SMAPEx-5 airborne instrument PLIS and considering the calculated β' and Γ parameters mentioned above through Eq. (1), and contrasted to that downscaled by the same process using backscatter from Sentinel-1, as archived in the NASA EarthData website (https://earthdata.nasa.gov).

3.3. Estimation of β' and Γ parameters

Fig. 5 shows the variation in $\beta'(C)$ for the four days of this campaign across pixel 1 and 2. The vegetation and soil roughness conditions have most effect on the magnitude of $\beta'(C)$ (Jagdhuber et al., 2018). As mentioned before and shown in Fig. 1, pixel 1 and 2 present heterogeneous land cover conditions which can lead to different magnitudes of $\beta'(C)$ for each day. The magnitudes for the L-L band combination were obtained as 4.45, 4.26, 3.56 and 3.06 for pixel 1 and 5.86, 5.84, 4.88 and 4.82 for pixel 2 from D1 to D8, while for the L-C band combination were 3.38 and 2.59 for pixel 1 for D3 and D8, respectively and 4.73, 3.83, 3.79 and 4.1 for pixel 2 from D1 to D8. The main vegetation types of SMAPEx-5 were cropping and grazing, with vegetation water contents increasing during D1 to D8 from 1.37 to 1.84 kg/m^2 for pixel 1 and 1.41 to 2.14 kg/m^2 for pixel 2, due to growth in the vegetation biomass during the three weeks long spring-time experiment. Das et al. (2019) and Jagdhuber et al. (2019a) showed that the β' parameter has a robust relation to vegetation water content, with reduced magnitude of β' for increased vegetation water content (VWC). In this study, the magnitude of β' estimations also decreased with higher values of vegetation water content (Fig. 5). However, the magnitudes of β' over pixel 2 were higher than pixel 1, with a change in β' of around 1.5 between the two pixels for each day. This may be explained by the greater heterogeneity and different land cover type of pixel 2, containing several patches of forest and a conservation area that are absent from pixel 1. The cross-polarized backscatter values were −24.00, −24.57, −24.53 and −24.81 dB across pixel 1, and −22.57, −23.89, −23.77 and −24.74 dB across pixel 2 at coarse resolution, while the co-polarized backscatter values were −13.96, −15.10, −16.05 and −16.06 dB across pixel 1, and −14.17, −15.43, −16.33 and −16.91 dB across pixel 2 at coarse resolution. Therefore, the dynamic range of backscatter across pixel 2 was larger compared with pixel 1, resulting in the higher vegetation structure parameter.

Consistent with the results from Jagdhuber et al. (2019b), it can also be seen that β' for both the C-L and L-L band combinations had limited sensitivity to soil moisture in high vegetation conditions. Fig. 5 shows that the β' magnitudes retrieved from C-band were less than L-band for each day. This is explained by increases in vegetation coverage leading to an increase in cross-polarized potential and decrease in covariation magnitude. These changes are stronger for the L-L band combinations than L-C band combinations of β' covariation because of higher canopy scattering for C-band (Jagdhuber et al., 2019a). It is notable that Sentinel didn't capture backscatter data for estimating β' of pixel 1 during D1 and D6.

The increasing of surface roughness also has an impact on reduction of β' magnitude. Previous research has shown that in low vegetation conditions, soil roughness causes a stronger reduction of β' magnitude for the L-C band combinations in contrast to the L-L band combinations (Jagdhuber et al., 2018). This means that surface roughness loss is greater at C-band compared to L-band due to the contribution from surface emission and scattering (Jagdhuber et al., 2019a). Overall, it can be said that the results using PLIS observations for estimation of β' through Eq. (2) matched with the results from Das et al. (2019).

The Γ values estimated using snapshots of PLIS σ_{vv} and σ_{vh} observations within each 36 km pixel ranged from 2.00 to 2.34 across pixel 1 and 2.28 to 2.92 across pixel 2. Globally, the mean values of Γ have been found to range from 2.5 to 4.5 (Das et al., 2019). Therefore, the results of Γ estimations from using σ_{vv} and σ_{vh} of PLIS closely follow the global values. It can be noted that the parameters (β' and Γ) derived on dates D1 and D6 for SMAP-Sentinel (L-C band) combination may not be optimal, as on those dates the Sentinel data only partially cover the SMAP 36 km grid cells.

4. Accuracy of downscaling

In this study, the vertical polarization of SMAP Level-2 brightness temperature with 36 km spatial resolution (L2_SM_P) was taken as the background *Tb*. The variation of σ_{vv} observations, aggregated to the downscaling resolution, was utilized to produce the higher resolution brightness temperature. In addition, σ_{vh} was considered as the indicator of vegetation impact because of strong correlation between cross-polarized backscatter and vegetation. Accordingly, the downscaled brightness temperature were retrieved from 36 km to 3 km and 9 km resolution from aggregating the 10 m resolution PLIS radar backscatter and Sentinel-1 observations to the target downscaling resolution. The method used for preparing the SMAP-PLIS downscaled *Tb* is the same as that used for preparing the SMAP-Sentinel downscaled *Tb* product. An alternate application of the method is to retrieve the downscaled *Tb* at fine resolution and then aggregate the downscaled *Tb* to 3 km and 9 km resolution. Wu et al. (2014) applied both methods and reported that both showed similar results. Finally, the downscaled *Tb* derived from combining the L-band SMAP radiometer and L-band PLIS radar observations, and that from the SMAP-Sentinel active-passive product were compared with the L-band *Tb* measured from PLMR, as a reference. As mentioned before, the SMAP-Sentinel active passive *Tb* is the product which NASA has utilized through combination of L-band SMAP *Tb* and C-band Sentinel-1 backscatter observations using the new baseline downscaling algorithm provided in Eq. (1).

4.1. Comparison between PLMR and SMAP brightness temperature

During SMAPEx-5, a total of 7 flights were undertaken coincident with SMAP overpasses. However in this study, only the information from 4 flights was considered due to the limited availability of Sentinel-1 data. The PLMR brightness temperature observations were aggregated from the 1 km original resolution to the 36 km SMAP coarse resolution pixel on these 4 days and compared with SMAP radiometer brightness temperature values on the selected area. As evidenced in Fig. 6, the

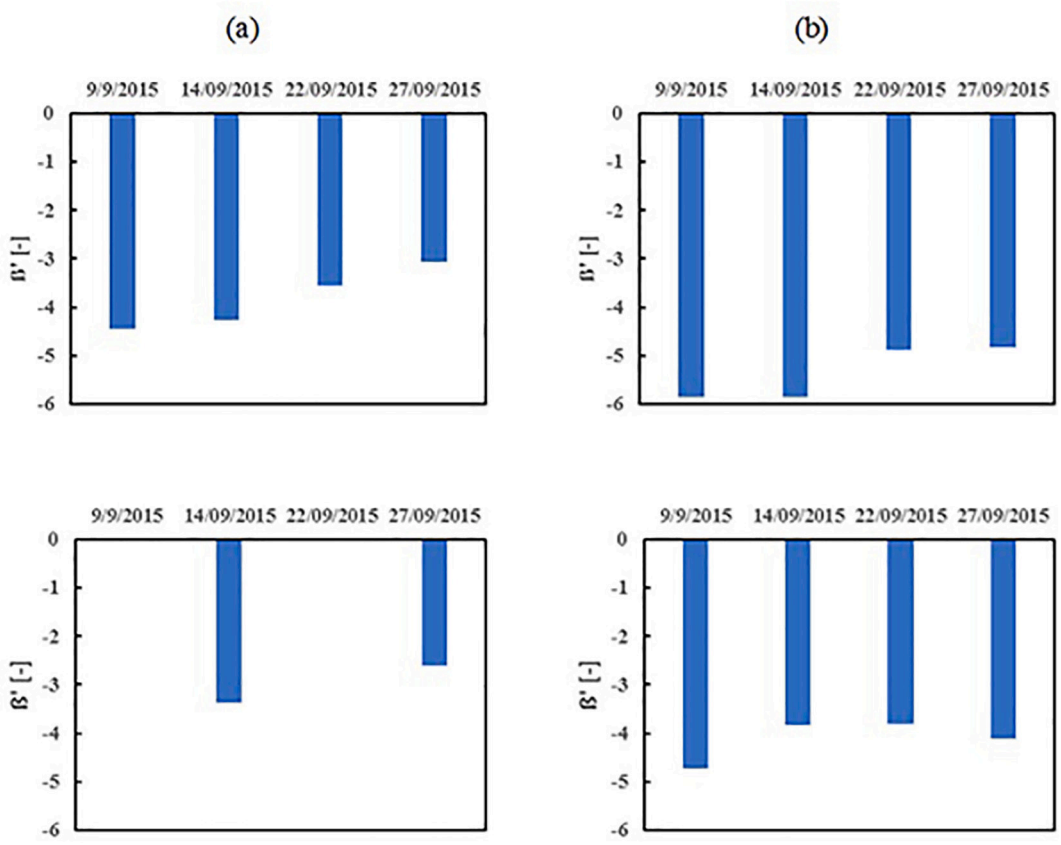

Fig. 5. Estimation of parameter *β′(C)* over a) pixel 1 and b) pixel 2 on the four days for SMAP-PLIS (L-L bands) combinations (top row) and SMAP-Sentinel (L-C bands) combinations (bottom row). Each pixel had a size of 36 km × 36 km.

comparison between the brightness temperature of PLMR and SMAP at 36 km resolution determined a bias of −3.2 K, *RMSE* of 3.6 K and correlation coefficient of 0.99. Consequently, in order to evaluate the downscaled brightness temperature algorithm, this bias was removed by subtracting the magnitude of the bias from all PLMR brightness temperature observations before using them as the independent reference in this study. This step was important, to ensure that differences between the downscaled *Tb* and reference observations of *Tb* at higher spatial resolution were the result of the downscaling algorithm and not due to sensor-to-sensor bias.

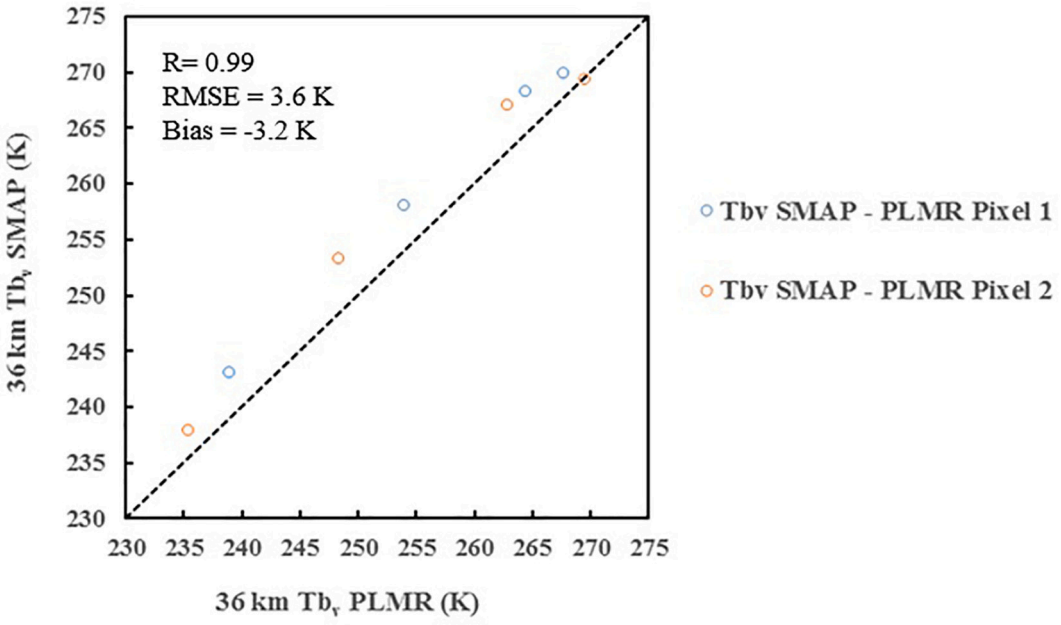

Fig. 6. Comparison between 36 km aggregated vertical *Tb* of PLMR and SMAP Level-2 vertical polarization brightness temperature (L2_SM_P) at 36 km resolution on two selected pixels across the 4 days.

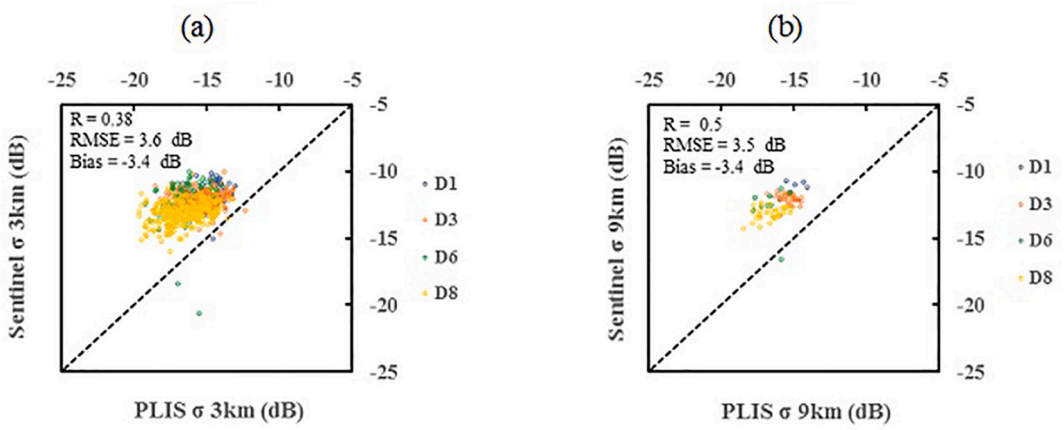

Fig. 7. Comparison between aggregated *vv*-polarization backscatter of PLIS and Sentinel 1A at EASE grid 3 km and 9 km resolutions over the study area across the 4 days.

4.2. Comparison between PLIS and Sentinel-1A backscatter observations

The Sentinel-1 spacecraft has a revisit interval time ranging from 6 to 12 days for different areas around the world. According to the Sentinel-1A overpass during the SMAPEx-5 campaign period, the backscatter observations were measured across 4 days at full or partial coverage over the selected study area, as shown in Fig. 2. The Sentinel-1A radar backscatter observations at 3 km resolution provided from the original NASA L2_S0_L1 product of Sentinel, were also aggregated to 9 km resolution. The comparison between aggregated PLIS σ_{vv} and Sentinel-1A σ_{vv} on the EASE-2 grid at 3 km and 9 km resolutions over the study area across the 4 days with coincident coverage are shown in Fig. 7. Through comparing pixel-by-pixel it can be seen that the magnitude of Sentinel-1A σ_{vv} was less than PLIS σ_{vv}, while the dynamic range of PLIS backscatter observations was higher than Sentinel-1A backscatter. The main reason for the difference between the magnitude of PLIS and Sentinel-1A SAR backscatter measurements is that the different frequency of L-band and C-band leads to differences in emission depths and the way the different wavelengths interact with the vegetation and surface roughness (El Hajj et al., 2018; Ulaby et al., 2019). It is noted that the overpass time of PLIS and Sentinel-1A is also different and that this can also have had an effect on the backscatter values, especially for D1 and D3 with 24 h time difference. Accordingly, it is expected that there will be some difference between PLIS and Sentinel-1A in Fig. 7, but as the main driver for the downscaling, it is useful to see the extent of this difference. Importantly, the day-to-day comparison between backscatter values shows a decrease from D1 to D8 for both C-band and L-band consistent with the soil moisture dry down across the 4 days.

4.3. Spatial and temporal variability of L-band and C-band downscaling

Based on the day-to-day estimation of β' at *v*-polarization and the Γ estimations described in the previous section, the new baseline downscaling algorithm was applied to downscale the brightness temperature for each of the four days using SMAP *Tb* and PLIS σ. Fig. 8a and b represent the vertically polarized brightness temperature maps of aggregated L-band SMAPEx-5 PLMR brightness temperature observations and the L-band and C-band SMAP downscaled brightness temperature data on the 3 km and 9 km EASE-2 grid. The pixel-by-pixel *Tb* absolute difference between downscaled brightness temperatures and PLMR *Tb* as the reference are also shown in Fig. 8. Importantly, the existence of urban areas, manmade structures and water bodies (Fig. 1) were successfully removed by the filtering process.

Generally, both the *Tb* downscaled SMAP-PLIS and *Tb* downscaled SMAP-Sentinel estimates had a similar temporal variation to the SMAPEx-5 airborne *Tb* from PLMR across the 4 days. While the heavy rainfall before starting the SMAPEx-5 campaign provided a heterogeneity in soil surface conditions, this reduced during the dry-down from D1 to D8, as clearly seen in the PLMR brightness temperature maps in Fig. 2. The plots of *Tb* downscaled SMAP-PLIS and *Tb* downscaled SMAP-Sentinel in Fig. 8 mirror this reduction in heterogeneity at both the 3 km and 9 km spatial resolutions, with more heterogeneous conditions during the first days of the campaign. Notably, D8 was the driest condition when compared to the other days. Moreover, based on the pixel-by-pixel absolute difference between *Tb* downscaled and *Tb* reference shown in Fig. 8, the results showed higher difference values for both C-band and L-band in pixels under higher soil moisture conditions. This can also result from the effect of heterogeneity in soil surface conditions on the downscaling algorithm. For example, the difference plots show that the downscaling errors were largest (29 K) at the southern part of pixel 1 and the eastern part of pixel 2 (3 km spatial resolution), being dominated by irrigated and dry cropping area with wet soil conditions. However, these differences reduced from D1 to D8 due to drying of the soil moisture with values of 15.5, 9.8 and 4.4 K for D3, D6 and D8, respectively. In contrast, 3 km grid cells with the lowest soil moisture during D1, located at the north west of pixel 1, had differences around 9 K. The results of this comparison show the large impact of soil moisture on downscaling errors.

Overall, comparison of the difference between *Tb* downscaled and *Tb* reference at the pixels with high soil moisture values showed that C-band presented higher error than L-band. This confirms the expectation that L-band has better ability for estimation of downscaled brightness temperature especially with heterogeneous soil conditions.

As shown in Fig. 1, the vegetation coverage of the selected area included irrigated and dry land cropping dominated by wheat in the eastern part of pixel 2 and the western part of pixel 1, grazing areas dominated by grassland in the central section, some forest area especially located in the northern part of pixel 2, and also some woodland along the Murrumbidgee River. Based on the difference between *Tb* downscaled and *Tb* reference shown in Fig. 8, the effects of vegetation cover on the downscaled brightness temperature achieved by the new baseline downscaling algorithm using C-band and L-band were investigated. Due to the maturity phase of crops during SMAPEx-5, the use of L-band backscatter in the downscaling algorithm showed better performance than C-band on the cropping area. This can be explained by the fact that the shorter wavelength C-band signals display stronger sensitivity than L-band to the vegetation cover. For instance, several cropping areas are located at the south western part of pixel 1. Considering D8 was the driest day and least affected by heterogeneous moisture conditions it is mostly affected by vegetation coverage. However, being later in the growing season the crop biomass and water

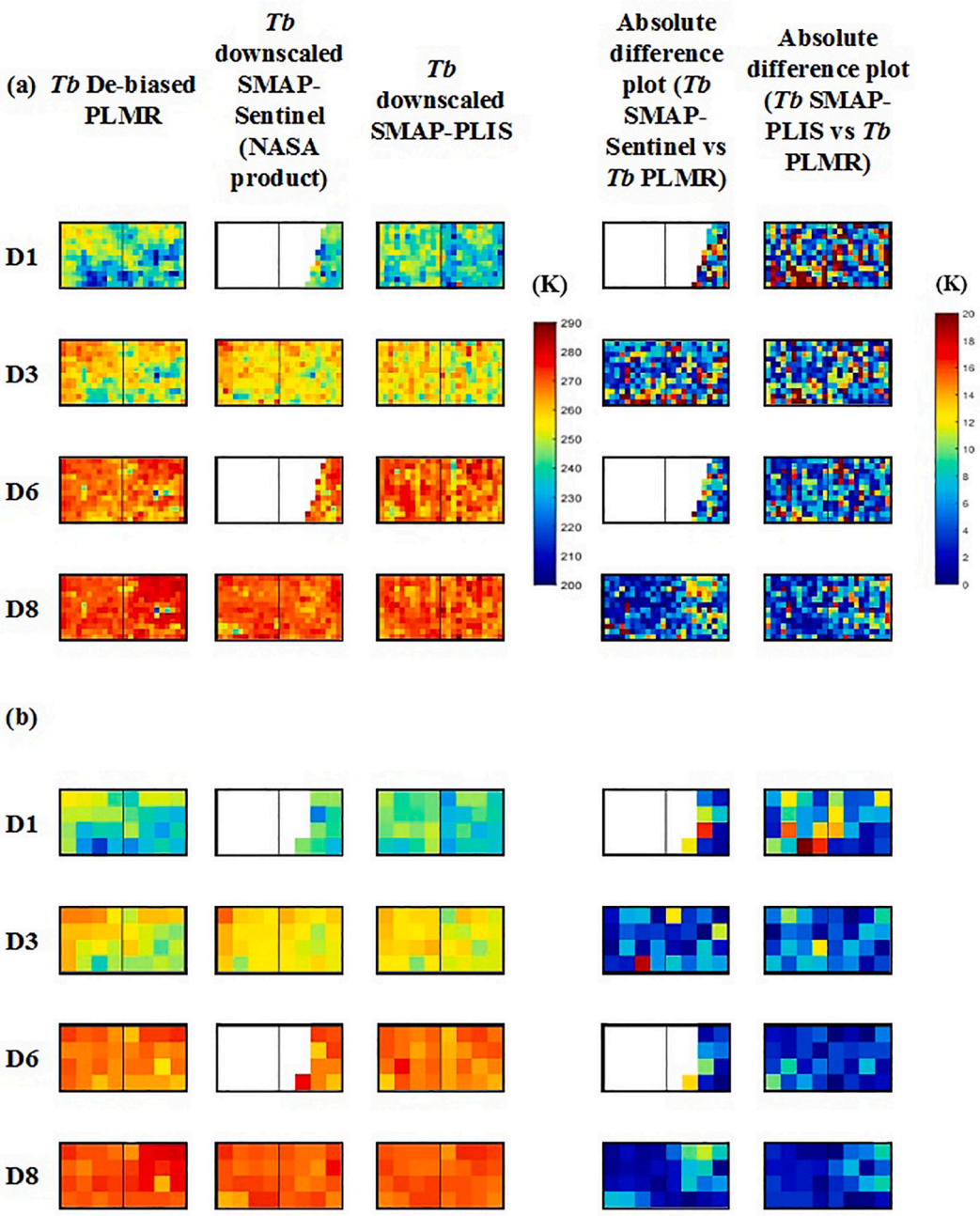

Fig. 8. Downscaling results at *v*-polarization across 4 days of SMAPEx-5 over selected pixels: reference PLMR *Tb*, *Tb* downscaled SMAP-Sentinel (NASA product), *Tb* downscaled SMAP-PLIS, and absolute difference between downscaled *Tb* SMAP-Sentinel and also, *Tb* SMAP-PLIS with reference *Tb*, a) at 3 km and b) 9 km spatial resolutions.

content was greatest, with both the 3 and 9 km difference plots in Fig. 8 showing lower errors for L-band (5.9 and 3.4 K) than C-band (8.8 and 7.6 K).

Similar to the cropping area, for dense grasses in grazing parts of selected pixels, the errors of the new baseline downscaling algorithm using L-band observations were lower than C-band. For example, the average of difference values between L-band *Tb* downscaled and *Tb* PLMR for several 3 km grid cells located in the grassland area at the central part of pixel 1 during D8 was 2.9 K, increasing to 3.3 K for C-band. Moreover, the difference values between *Tb* downscaled and *Tb* PLMR for one of the 9 km spatial resolution pixels located at the central part of pixel 1 and dominantly covered by grasslands were 1.5 K and 1.9 K for L-band and C-band, respectively on D8. For the pixels covered by forest canopy and woodland, L-band also showed better performance due to the higher ability to penetrate the dense vegetation coverage. Investigation on the forest area located at the northern part of pixel 2 showed that the average difference value between L-band *Tb* downscaled and *Tb* PLMR for 3 km grid cells located at this forest part during D8 were 5.8 K, and increased to 11.5 K for C-band. Furthermore, the average of difference values across the 4 days for two 9 km grid cells located at this forest area were 5.1 K and 10.3 K for L-band and C-band, respectively. Therefore, the downscaled brightness temperature of C-band observations has shown a higher difference with regard to the reference brightness temperature spatially at the northern part of pixel 2. It is also notable that the heterogeneous land cover conditions of pixel 2 were higher than pixel 1, leading to more variation in the difference plots, as can be seen in Fig. 8 at 3 km and 9 km spatial resolution.

Table 2
Accuracy of the SMAP baseline downscaling algorithm; Root mean square error (*RMSE*)/Correlation coefficient (*R*)/Bias between L-band downscaled *Tb* (SMAP-PLIS) and de-biased L-band PLMR *Tb*, and between *Tb* SMAP-Sentinel (NASA product) and de-biased *Tb* PLMR across the 4-days (D1, D3, D6, D8) averaged over the entire study area (pixel 1 and 2), with the analysis for all 4 of the days shown in the last column. The *RMSE* and Bias values are in K. The rows 1, 2 and 3 present *RMSE*, *R* and Bias, respectively.

Downscaling resolution (km)	Downscaling product	D1	D3	D6	D8	All days
3	SMAP-PLIS	11.4/	10.2/	8.3/	7.9/	9.4/
		0.44/	0.34/	0.36/	0.18/	0.75/
		1.9	−0.77	−0.85	2	0.6
	SMAP-Sentinel	12.1/	10.5/	8.7/	8.3/	9.7/
		0.43/	0.32/	0.43/	0.06/	0.72/
		−1.83	−2.2	−0.74	2.1	−0.3
9	SMAP-PLIS	5.9/	5.8/	3.9/	3.9/	4.9/
		0.60/	0.63/	0.76/	0.44/	0.92/
		−0.09	−0.7	−1.67	1.9	0.3
	SMAP-Sentinel	8.4/	6.2/	6.3/	4.8/	6.0/
		0.39/	0.63/	0.35/	0.15/	0.88/
		−2.6	−2.2	−1.9	2.1	−0.5

In order to assess the new baseline downscaling algorithm, the SMAP-PLIS and SMAP-Sentinel downscaled brightness temperature estimations were compared with PLMR *Tb* at the pixel level at 3 km and 9 km resolution, with *RMSE*, bias and correlation coefficient (*R*) calculated over the study area for each day. Table 2 shows the accuracy of the downscaling algorithm on each day of the campaign over the study area for 3 km and 9 km resolutions at vertical polarization. The results show the higher correlation coefficient of SMAP downscaled brightness temperature estimates for L-band than C-band. Taking the aggregated PLMR *Tb* as the independent reference, the *RMSE* was calculated for brightness temperature estimates on each day. It can obviously be seen from Table 2 that the results of the downscaling algorithm using L-band backscatter have shown lower *RMSE* than C-band for each day. Generally, the *RMSE* of L-band comparing day-to-day with C-band have decreased by around 0.3 to 0.7 K at 3 km, and decreased by around 0.4 to 2.5 K at 9 km spatial resolution across D1 to D8. The *RMSE* results of the new baseline algorithm in downscaling the brightness temperature for D1 and D3 displayed relatively poorer performance than D6 and D8 for both L-band and C-band at 3 km and 9 km resolutions. This can be explained by the heterogeneous soil surface conditions which occurred because of the heavy rainfall events before the beginning of the SMAPEx-5 campaign, and decreased as the campaign progressed. Moreover, the *RMSE* reduced when the spatial resolution decreased from 3 km to 9 km. In other words, changing from coarse to fine spatial resolution reduced the accuracy of the downscaled brightness temperature. This can be associated with the increase in backscatter noise and soil surface heterogeneity both in terms of soil moisture and vegetation at finer resolution.

4.4. Impact of C-band and L-band on the downscaling performance

For the purpose of performance assessment of the new baseline downscaling algorithm, the SMAP-PLIS and SMAP-Sentinel downscaled brightness temperature estimations were compared with PLMR *Tb* at the pixel level in Fig. 9 respectively. The statistical results including *RMSE*, bias and correlation coefficient (*R*) calculated across the four days over the study area are shown in Table 2. The statistics indicate that the L-band SMAP-PLIS downscaled brightness temperature estimates had a correlation of 0.75 and 0.92, and bias of 0.6 K and 0.3 K, when compared with PLMR brightness temperature observations at both 3 km and 9 km spatial resolutions. This can be compared to downscaled brightness temperature of the SMAP L2_SM_SP product for C-band SMAP-Sentinel. Accordingly, the SMAP-PLIS downscaled brightness temperature estimates had a lower *RMSE* than SMAP-Sentinel *Tb* at both 3 km and 9 km spatial resolution, with a 0.3 K improvement at 3 km and 1.1 K improvement at 9 km.

In order to differentiate the impact of C-band SAR and L-band SAR on the downscaling performance, considering the land use and cover types, the spatial distribution of temporal average *RMSE* and correlation coefficient of all 4 days was computed at different resolutions across the whole study area in Figs. 10 and 11. Both *RMSE* and *R* were computed from the time series of downscaled brightness temperature and reference brightness temperature at each pixel across the 4 days, and at two resolution levels: 3 km and 9 km. It is notable that SMAP-Sentinel brightness temperature data was not available at full coverage for D1 and D6. Therefore, the spatial maps of temporal *RMSE* and *R* only have partial coverage of the selected area, which is dominated by cropland and some forest area at the northern part of pixel 2.

As shown in Fig. 10, based on the available pixels, the *RMSE* values between *Tb* downscaled and *Tb* reference were generally lower at L-band than C-band. This means that L-band had a better downscaling performance than C-band for croplands, forests and woodlands. It can be noted that the existing noise produced by radar in croplands was more than for other surface coverages since croplands showed more variation in the vegetation and surface roughness conditions. Accordingly, considering these radar data, the croplands produce an obstacle for the accuracy of downscaling. Moreover, the estimation of SMAP downscaled brightness temperature displayed high correlation to PLMR observations across the 4 days observed brightness temperature over the study area for both C-band and L-band. However, as shown in Fig. 11, L-band downscaled brightness temperature had higher correlation than C-band with PLMR brightness temperature in croplands and forest conditions. This is because of the increased capability of L-band to penetrate the crop and forest.

5. Conclusions

The soil moisture active passive (SMAP) satellite launched by NASA on 31st January 2015, intended to provide global soil moisture maps at 9 km spatial resolution by downscaling L- band radiometer brightness temperature with L-band radar backscatter, obtained at 36 km and 3 km spatial resolution respectively. However, SMAP's radar ended its operation prematurely due to a technical problem and NASA focused on other active microwave satellites, ultimately selecting the C-band Sentinel-1A/1B SAR data as an alternative for the SMAP L-band radar. The objective of this study was to investigate the impact of using C-band in place of L-band in downscaling the brightness temperature. The new SMAP baseline downscaling algorithm was utilized to downscale SMAP brightness temperature using L-band airborne radar backscatter (PLIS) from the SMAPEx-5 field campaign in Australia, to spatial resolutions of 3 km and 9 km at vertical polarization. The downscaled *Tb* was evaluated by L-band observed airborne *Tb* from the SMAPEx-5 (PLMR) and contrasted against the C-band downscaled *Tb*. The SMAP-Sentinel brightness temperature active passive product which is provided by NASA using combination of L-band SMAP *Tb* and C-band Sentinel-1 backscatter observations was considered for this purpose.

The average *RMSE*, correlation coefficient and bias of downscaled *Tb* compared with *Tb* of PLMR as a reference data across 4 days at 9 km resolution were 4.9 K, 0.92 and 0.3 K for L-band and 6 K, 0.88 and −0.5 K for C-band, and increased to 9.4 K, 0.75 and 0.6 K for L-band and 9.7 K, 0.72 and −0.3 K for C-band at 3 km spatial resolution. The *RMSE* over the 4 days at L-band comparing with C-band decreased by 0.3 K at 3 km, and by 1.1 K at 9 km spatial resolution. Moreover, when considering the statistical analysis for each day separately, it was found that the new baseline downscaling algorithm performed poorly in the early days of the campaign for both L-band and C-band as a result of high soil moisture leading to large spatial heterogeneity. Results showed an increase in the algorithm performance during the drying down period, with an *RMSE* better than 3.5 K for L-band at 3 km spatial resolution. Overall, there were better results for the L-band comparison

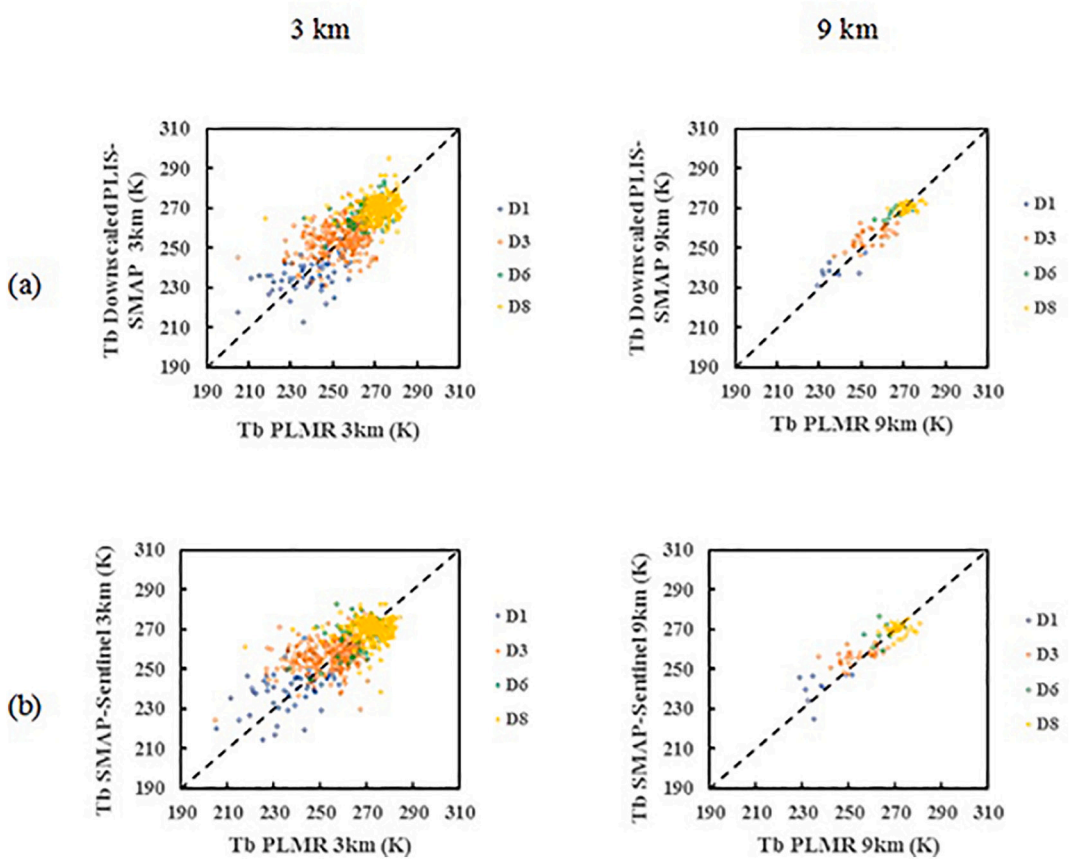

Fig. 9. Comparison between a) *Tb* downscaled SMAP-PLIS and *Tb* PLMR, and b) *Tb* SMAP-Sentinel and *Tb* PLMR during SMAPEx-5 across 4 days at 3 km and 9 km resolution at vertical polarization.

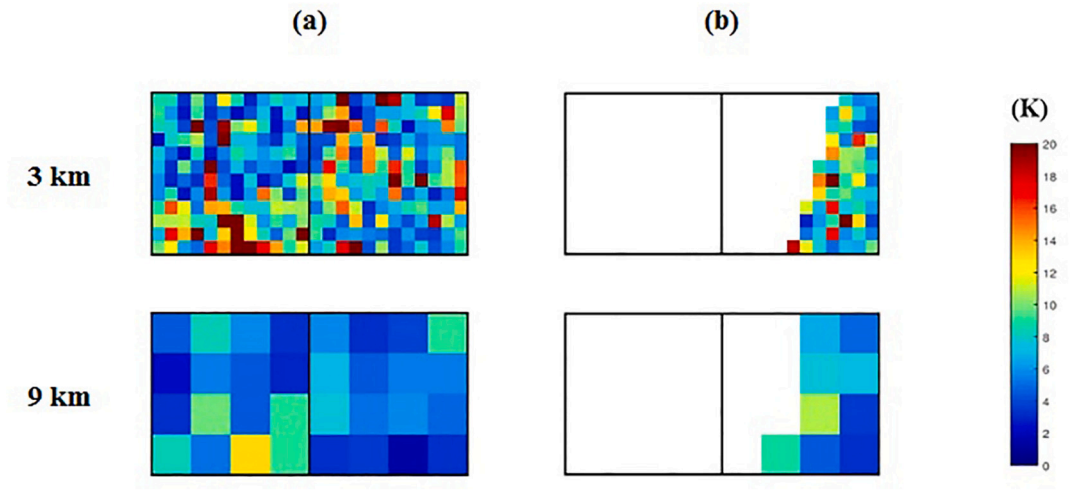

Fig. 10. Spatial maps of temporal *RMSE* between PLMR brightness temperature observations as the reference and a) SMAP-PLIS downscaled brightness temperature estimates and b) SMAP-Sentinel brightness temperature, in vertical polarization over the selected pixel 1 and 2 during SMAPEx-5 at 3 km and 9 km resolution.

than C-band for all days at 3 km and 9 km spatial resolution. Based on the fact that 3 K error of brightness temperature is generally expected to translate to approximately 0.01 m^3/m^3 additional soil moisture estimation error (De Lannoy and Reichle, 2016), the use of C-band backscatter in place of L-band backscatter is expected to result in less than 0.01 m^3/m^3 error in soil moisture estimates.

Accordingly, it can be said that generally the performance of the new version of the baseline downscaling algorithm is better when used with L-band than C-band, but these differences can be expected to have a minor impact on results. However, there are several sources of difference between using L-band and C-band radar observations in the downscaling algorithm which effect the results. L-band and C-band represent different emission depths due to their different frequency. Moreover, the land cover type and surface heterogeneity have a greater impact on the C-band backscatter than at L-band. Therefore, the disadvantage of using Sentinel-1 observations is that there is a greater sensitivity to vegetation. Overall, the results of this study clearly show that the L-band backscatter provided satisfactory downscaling results at 9 km resolution.

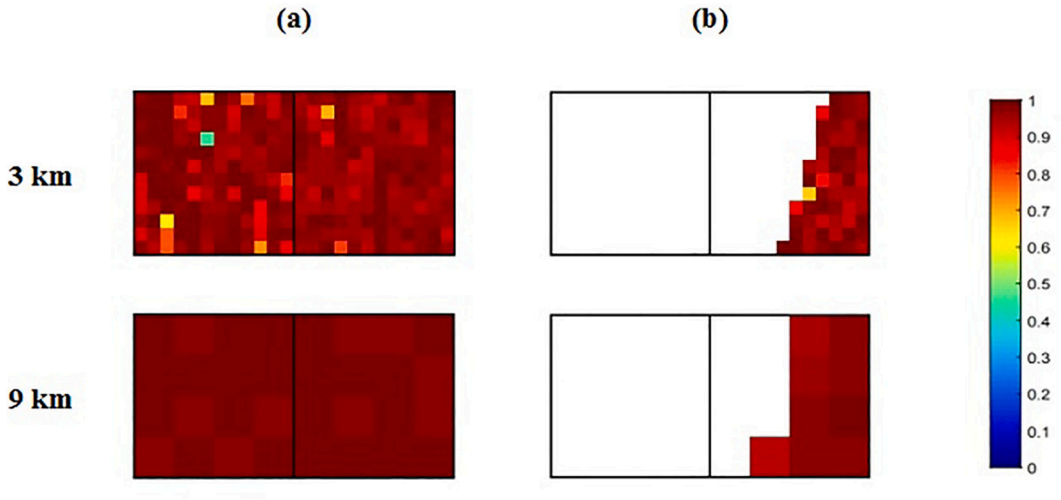

Fig. 11. Spatial maps of temporal correlation coefficient between PLMR brightness temperature observations as the reference and a) SMAP-PLIS downscaled brightness temperature and b) SMAP-Sentinel brightness temperature, in vertical polarization over the selected pixel 1 and 2 during SMAPEx-5 at 3 km and 9 km resolution.

Declaration of Competing Interest

None.

Acknowledgments

The SMAPEx field campaigns and related research development have been funded by the Australian Research Council Discovery (DP140100572) and Australian Research Council Linkage Infrastructure Equipment and Facilities grants (LE0882509 and LE0453434). Monash University is also acknowledged for its contribution and support of Elaheh Ghafari to complete this research.

References

Chan, S.K., Bindlish, R., Neill, P.E.O., Njoku, E., Jackson, T., Colliander, A., Chen, F., Burgin, M., Dunbar, S., Piepmeier, J., Yueh, S., Entekhabi, D., Cosh, M.H., Caldwell, T., Walker, J., Wu, X., Berg, A., Rowlandson, T., Pacheco, A., McNairn, H., Thibeault, M., Martínez-Fernández, J., Á, G.-Z., Seyfried, M., Bosch, D., Starks, P., Goodrich, D., Prueger, J., Palecki, M., Small, E.E., Zreda, M., Calvet, J., Crow, W.T., Kerr, Y., 2016. Assessment of the SMAP passive soil moisture product. IEEE Trans. Geosci. Remote Sens. 54, 4994–5007.

Colliander, A., Jackson, T.J., Bindlish, R., Chan, S., Das, N., Kim, S.B., Cosh, M., Dunbar, R.S., Dang, L., Pashaian, L., Asanuma, J., Aida, K., Berg, A., Rowlandson, T., Bosch, D., Caldwell, T., Caylor, K., Goodrich, D., Aljassar, H.K., Yueh, S., 2017. Validation of SMAP surface soil moisture products with core validation sites. Remote Sens. Environ. 191, 215–231.

Das, N., Dunbar, R.S., 2017. Level2 SMAP/Sentinel Active/Passive Soil Moisture Product Specification Document.

Das, N., Entekhabi, D., Njoku, E., 2011. An Algorithm for Merging SMAP Radiometer and Radar Data for High-resolution Soil-moisture Retrieval.

Das, N.N., Entekhabi, D., Njoku, E.G., Shi, J.J.C., Johnson, J.T., Colliander, A., 2014. Tests of the SMAP combined radar and radiometer algorithm using airborne field campaign observations and simulated data. IEEE Trans. Geosci. Remote Sens. 52, 2018–2028.

Das, N.N., Entekhabi, D., Dunbar, R.S., Colliander, A., Chen, F., Crow, W., Jackson, T.J., Berg, A., Bosch, D.D., Caldwell, T., Cosh, M.H., Collins, C.H., Lopez-Baeza, E., Moghaddam, M., Rowlandson, T., Starks, P.J., Thibeault, M., Walker, J.P., Wu, X., O'Neill, P.E., Yueh, S., Njoku, E.G., 2018. The SMAP mission combined active-passive soil moisture product at 9 km and 3 km spatial resolutions. Remote Sens. Environ. 211, 204–217.

Das, N.N., Entekhabi, D., Dunbar, R.S., Chaubell, M.J., Colliander, A., Yueh, S., Jagdhuber, T., Chen, F., Crow, W., O'Neill, P.E., Walker, J.P., Berg, A., Bosch, D.D., Caldwell, T., Cosh, M.H., Collins, C.H., Lopez-Baeza, E., Thibeault, M., 2019. The SMAP and Copernicus Sentinel 1A/B microwave active-passive high resolution surface soil moisture product. Remote Sens. Environ. 233, 111380.

De Lannoy, G.J.M., Reichle, R.H., 2016. Assimilation of SMOS brightness temperatures or soil moisture retrievals into a land surface model. Hydrol. Earth Syst. Sci. 20, 4895–4911.

El Hajj, M., Baghdadi, N., Bazzi, H., Zribi, M., 2018. Penetration analysis of SAR signals in the C and L bands for wheat, maize, and grasslands. Remote Sens. 11, 31.

Entekhabi, D., Njoku, E., O'Neill, P., Kellogg, K.H., Crow, W., Edelstein, W.N., Entin, J., Goodman, S., Jackson, T., Johnson, J., Kimball, J., Piepmeier, J., Koster, R., Martin, N., McDonald, K., Moghaddam, M., Moran, S., Reichle, R., Shi, J., van Zyl, J., 2010. The Soil Moisture Active and Passive (SMAP) Mission.

Entekhabi, D., Yueh, S., O'Neill, P.E., Kellogg, K.H., Allen, A., Bindlish, R., Brown, M., Chan, S., Colliander, A., Crow, W.T., Das, N., De Lannoy, G., Dunbar, R.S., Edelstein, W.N., Entin, J.K., Escobar, V., Goodman, S.D., Jackson, T.J., Jai, B., Johnson, J., Kim, E., Kim, S., Kimball, J., Koster, R.D., Leon, A., McDonald, K.C., Moghaddam, M., Mohammed, P., Moran, S., Njoku, E.G., Piepmeier, J.R., Reichle, R., Rogez, F., Shi, J.C., Spencer, M.W., Thurman, S.W., Tsang, L., Van Zyl, J., Weiss, B., West, R., 2014. SMAP Handbook–Soil Moisture Active Passive: Mapping Soil Moisture and Freeze/Thaw from Space.

Falloon, P., Jones, C.D., Ades, M., Paul, K., 2011. Direct soil moisture controls of future global soil carbon changes: an important source of uncertainty. Glob. Biogeochem. Cycles 25.

Jagdhuber, T., Entekhabi, D., Das, N.N., Link, M., Montzka, C., Kim, S., Yueh, S., 2017. Microwave covariation modeling and retrieval for the dual-frequency active-passive combination of sentinel-1 and SMAP. In: 2017 IEEE International Geoscience and Remote Sensing Symposium (IGARSS), pp. 3996–3999.

Jagdhuber, T., Entekhabi, D., Das, N., Link, M., Baur, M., Akbar, R., Montzka, C., Kim, S., Yueh, S., Baris, I., 2018. Physics-based modeling of active-passive microwave covariations for geophysical retrievals. In: IGARSS 2018–2018 IEEE International Geoscience and Remote Sensing Symposium, pp. 250–253.

Jagdhuber, T., Baur, M., Akbar, R., Das, N.N., Link, M., He, L., Entekhabi, D., 2019a. Estimation of active-passive microwave covariation using SMAP and Sentinel-1 data. Remote Sens. Environ. 225, 458–468.

Jagdhuber, T., Konings, A.G., McColl, K.A., Alemohammad, S.H., Das, N.N., Montzka, C., Link, M., Akbar, R., Entekhabi, D., 2019b. Physics-based modeling of active and passive microwave covariations over vegetated surfaces. IEEE Trans. Geosci. Remote Sens. 57, 788–802.

Jian, P., Alexander, L., Olivier, M., C., V.N.E., 2017. A review of spatial downscaling of satellite remotely sensed soil moisture. Rev. Geophys. 55, 341–366.

Kerr, Y.H., Waldteufel, P., Richaume, P., Wigneron, J.P., Ferrazzoli, P., Mahmoodi, A., Bitar, A.A., Cabot, F., Gruhier, C., Juglea, S.E., Leroux, D., Mialon, A., Delwart, S., 2012. The SMOS soil moisture retrieval algorithm. IEEE Trans. Geosci. Remote Sens. 50, 1384–1403.

Leese, J., Jackson, T., Pitman, A., Dirmeyer, P., 2001. Meeting Summary: GEWEX/BAHC International Workshop on Soil Moisture Monitoring, Analysis, and Prediction for Hydrometeorological and Hydroclimatological Applications.

Narayan, U., Lakshmi, V., Jackson, T.J., 2006. High-resolution change estimation of soil moisture using L-band radiometer and radar observations made during the SMEX02 experiments. IEEE Trans. Geosci. Remote Sens. 44, 1545–1554.

Panciera, R., Walker, J.P., Jackson, T.J., Gray, D.A., Tanase, M.A., Ryu, D., Monerris, A., Yardley, H., Rüdiger, C., Wu, X., Gao, Y., Hacker, J.M., 2014. The soil moisture active passive experiments (SMAPEx): toward soil moisture retrieval from the SMAP mission. IEEE Trans. Geosci. Remote Sens. 52, 490–507.

Piles, M., Entekhabi, D., Camps, A., 2009. A change detection algorithm for retrieving high-resolution soil moisture from SMAP radar and radiometer observations. IEEE Trans. Geosci. Remote Sens. 47, 4125–4131.

Sabaghy, S., Walker, J.P., Renzullo, L.J., Jackson, T.J., 2018. Spatially enhanced passive microwave derived soil moisture: capabilities and opportunities. Remote Sens. Environ. 209, 551–580.

Sabaghy, S., Walker, J.P., Renzullo, L.J., Akbar, R., Chan, S., Chaubell, J., Das, N., Dunbar, R.S., Entekhabi, D., Gevaert, A., Jackson, T.J., Loew, A., Merlin, O., Moghaddam, M., Peng, J., Peng, J., Piepmeier, J., Rüdiger, C., Stefan, V., Wu, X., Ye, N., Yueh, S., 2020. Comprehensive analysis of alternative downscaled soil moisture

products. Remote Sens. Environ. 239, 111586.
Seneviratne, S.I., Corti, T., Davin, E.L., Hirschi, M., Jaeger, E.B., Lehner, I., Orlowsky, B., Teuling, A.J., 2010. Investigating soil moisture–climate interactions in a changing climate: a review. Earth Sci. Rev. 99, 125–161.
Torres, R., Snoeij, P., Geudtner, D., Bibby, D., Davidson, M., Attema, E., Potin, P., Rommen, B., Floury, N., Brown, M., Traver, I.N., Deghaye, P., Duesmann, B., Rosich, B., Miranda, N., Bruno, C., L'Abbate, M., Croci, R., Pietropaolo, A., Huchler, M., Rostan, F., 2012. GMES Sentinel-1 mission. Remote Sens. Environ. 120, 9–24.
Ulaby, F.T., Moore, R.K., Fung, A.K., 1981. Microwave Remote Sensing Active and Passive-volume I: Microwave Remote Sensing Fundamentals and Radiometry.
Ulaby, F., Dobson, M.C., Álvarez-Pérez, J.L., 2019. Handbook of Radar Scattering Statistics for Terrain. Artech House.
Walker, J.P., Houser, P.R., 2004. Requirements of a global near-surface soil moisture satellite mission: accuracy, repeat time, and spatial resolution. Adv. Water Resour. 27, 785–801.
Wu, X., Walker, J.P., Das, N.N., Panciera, R., Rüdiger, C., 2014. Evaluation of the SMAP brightness temperature downscaling algorithm using active–passive microwave observations. Remote Sens. Environ. 155, 210–221.
Wu, X., Walker, J.P., Rüdiger, C., Panciera, R., Gray, D.A., 2015. Simulation of the SMAP data stream from SMAPEx field campaigns in Australia. IEEE Trans. Geosci. Remote Sens. 53, 1921–1934.
Xiwu, Z., Houser, P.R., Walker, J.P., Crow, W.T., 2006. A method for retrieving high-resolution surface soil moisture from hydros L-band radiometer and Radar observations. IEEE Trans. Geosci. Remote Sens. 44, 1534–1544.
Ye, N., Walker, J.P., Rüdiger, C., 2015. A cumulative distribution function method for normalizing variable-angle microwave observations. IEEE Trans. Geosci. Remote Sens. 53, 3906–3916.
Ye, N., Walker, J.P., Bindlish, R., Chaubell, J., Das, N.N., Gevaert, A.I., Jackson, T.J., Rüdiger, C., 2019. Evaluation of SMAP downscaled brightness temperature using SMAPEx-4/5 airborne observations. Remote Sens. Environ. 221, 363–372.
Ye, N., Walker, J.P., Wu, X., Jeu, R.d., Gao, Y., Jackson, T.J., Jonard, F., Kim, E., Merlin, O., Pauwels, V.R.N., Renzullo, L.J., Rüdiger, C., Sabaghy, S., Hebel, C.v., Yueh, S.H., Zhu, L., 2020. The soil moisture active passive experiments: validation of the SMAP products in Australia. IEEE Trans. Geosci. Remote Sens. 1–18.
Yueh, S., Entekhabi, D., Neill, P.O., Njoku, E., Entin, J., 2016. NASA Soil Moisture Active Passive mission status and science performance. In: 2016 IEEE International Geoscience and Remote Sensing Symposium (IGARSS), pp. 116–119.
Zhu, L., Walker, J.P., Ye, N., Rüdiger, C., Hacker, J.M., Panciera, R., Tanase, M.A., Wu, X., Gray, D.A., Stacy, N., Goh, A., Yardley, H., Mead, J., 2018. The polarimetric L-band imaging synthetic aperture radar (PLIS): description, calibration, and cross-validation. IEEE J. Select. Topics Appl. Earth Observ. Remote Sens. 11, 4513–4525.